

The Aerosol Limb Imager: Acousto-Optic 2D Measurements of Limb Scattered Sunlight for Stratospheric Aerosol Profiling

Brenden J Elash, Adam E Bourassa, Paul R P Loewen, Douglas A Degenstein

August 13, 2015

Abstract

The Aerosol Limb Imager (ALI) is a remote sensing instrument designed to measure scattered sunlight from the atmospheric limb to retrieve spatially resolved information of the stratospheric aerosol distribution, including extinction coefficient and particle size. The long term goal of this work is the eventual realization of ALI on a satellite platform in low earth orbit. Here we present the development of an ALI prototype and the results from a test flight on a stratospheric balloon. The ALI instrument concept uses a large aperture Acousto-Optical Tunable Filter (AOTF) to successively image the stratospheric limb in a selectable narrow wavelength band ranging from the visible to the near infrared. The afocal optical system design uses telescopic front end optics to pass collimated light through the AOTF for each line-of-sight, which provides robust imaging that is relatively insensitive to impurities in the AOTF, at the cost of a small spectral gradient in the measured image that is negligible for the broad band aerosol spectral scattering characteristic. The ALI prototype was tested on a stratospheric balloon flight from the Canadian Space Agency (CSA) launch facility in Timmins, Canada, in September, 2014. Preliminary analysis of hyperspectral images indicate that the radiance measurements are high quality and can be used to retrieve vertical profiles of stratospheric aerosol extinction coefficient and one moment of the particle size distribution.

1 Introduction

Stratospheric aerosol plays a fundamental role in the global climate balance. It is generally a spherical particle consisting of hydrated droplets of sulfuric acid that scatters incoming solar radiation away from the surface of the planet causing an overall cooling effect which is dependant on extinction and particle size distribution (*Kiehl and Briegleb, 1993*). This effect is fully defined by aerosol microphysics and requires accurate knowledge of concentration and particle size distributions. Stratospheric aerosol loading has been increasing at a rate of 4-7% per year from 2002 to 2009 due to moderate volcanic eruptions (*Vernier et al., 2011*). There has also been a 5.2% increase per year from 2002 to 2007 to the surface SO₂ emissions level which may have lead to an increase in the background stratospheric aerosol layer (*Hofmann et al., 2009*). The negative radiative effect from this increase has potentially partially offset the radiative forcing from CO₂ (*Solomon et al., 2011*). During the anticyclone of the asian summer monsoon an aerosol layer forms known as the Asian Tropopause Aerosol Layer (ATAL). The ATAL is located in the monsoon's large scale anticyclone circulation and the monsoon propels atmospheric constituents upwards and isolates them from the external environment. The Asian monsoon can also inject anthropogenic sources of SO₂ which enter the stratosphere through the ATAL that forms during the Asian monsoon (*Vernier et al., 2011; Neely et al., 2014*). Also, the 2011 eruption of Nabro ejected SO₂ into the troposphere which was transported into the anticyclone of the asian monsoon. The monsoon vertically transported the aerosol across the tropopause into the stratosphere (*Bourassa et al., 2012*).

Aerosol in the stratosphere has been monitored from satellite platforms throughout the last few decades. Solar occultation has been used since the 1970s to monitor aerosol in the stratosphere and has provided a reliable, accurate and long term database of background and volcanic aerosol extinctions. Notable occultation instruments include SAM II (*McCormick et al., 1979*), SAGE II (*McCormick, 1987*), and SAGE III (*Thomason and Taha, 2003*) and their combined life cycles gathered measurements from 1978 to 2005. The occultation method has the ability to self-calibrate each measurement by directly viewing the sun outside of the atmosphere. The method also directly measures the optical depth allowing for simple conversion to extinction without the need for particle size knowledge.

More recently the limb scatter technique, which measures scattered radiance from the sun-

lit atmosphere, has been used to determine aerosol extinction. Although this geometry has the advantage of being able to measure the atmosphere throughout the sunlit conditions, unlike occultation which can only gather measurements during sunrise or sunset events, the scattering process requires the use of a forward model to retrieve atmospheric parameters, making the inversion process from limb scatter measurements computationally heavy and time intensive. Limb scatter was first performed on the Solar Mesosphere Explorer (SME) (*Barth et al.*, 1983) to measure ozone profiles and was followed in the 2000s by instruments with the ability to measure aerosol. The Optical Spectrograph and InfraRed Imaging System (OSIRIS) a Canadian instrument onboard the Odin satellite (*Llewellyn et al.*, 2004) and SCanning Imaging Absorption spectroMeter for Atmospheric CHartographY (SCIAMACHY) onboard the ENVISAT (*Bovensmann et al.*, 1999) are two limb scatter instruments have successfully determined aerosol atmospheric parameters. OSIRIS has a version 5 data product that contains 750 nm aerosol extinction with a 1 km vertical resolution (*Bourassa et al.*, 2012b) and was retrieved using the Multiplicative Algebraic Relaxation Technique (MART) method (*Degenstein et al.*, 2009) and SCIAMACHY uses an optimal estimation method to also retrieve 750 nm aerosol extinction profiles (*Ernst et al.*, 2012). These instruments are grating spectrometers with a single line of sight that acquire spectra at a single tangent altitude at a time so a series of exposures is required to create a vertical profile. With approximately a 1.5 km and 3 km vertical resolution for OSIRIS and SCIAMACHY respectively. The Ozone Mapping Profiler Suite - Limb Profiler (OMPS-LP) (*Rault and Loughman*, 2013), launched in 2012, uses a prism to disperse the light and images the atmosphere through three verticals slits. Each slit images 100 km vertically with a 1.5 km vertical resolution. The center slit looks backward along the satellite track while the other two slits are offset by 4.25° horizontally. The aerosol product for OMPS is retrieved using optimal estimation at wavelengths of 513, 671, 746, 870, and 920 nm with 1 km vertical resolution.

A lidar instrument, CALIPSO, measures the atmosphere with profiles of 333 m horizontal resolution and 60 m, 180 m, and 300 m vertical resolution for the altitude ranges of 8.2-20.2 km, 20.2-30.1 km, and 30.1-40.0 km respectively (*Winker et al.*, 2003). The stratospheric aerosol has been used in studies with a 16 day averaged 3-D grid with a resolution of 1° latitude by 2° longitude by 200 m vertically. Each aerosol data cell is the average of 300 to

600 profiles (*Vernier et al.*, 2009). Additional instrumentation with high resolutions on the order of 200 m vertically will satisfy the needs for current scientific investigation and will allow the determination of aerosol loading. Furthermore, there is a decrease in the number of satellites performing remote sensing of the atmosphere, newer instruments that fill the scientific requirements are required in order to replace these deficiencies.

ALI will address the much needed horizontal and vertical resolution on the orders of hundreds of meters which is required to better understand aerosol transportation and climate effects. ALI will use the limb scatter geometry to gather 2-D spatial images of the atmosphere and gather spectral information by taking measurements at different wavelengths using an Acousto-Optic Tunable Filter (AOTF). An AOTF is a device that allows the change of a filtering wavelength without any moving parts and low power consumption. AOTFs operate efficiently in the Near InfraRed (NIR) which is an excellent wavelength range for sensitivity to aerosol signal (*Rieger et al.*, 2014). Inherently, AOTFs can only filter linear polarized light resulting in ALI only being able to measure a single polarization. Further the bandpass of the AOTF, approximately 2 nm at 600 nm and 7 nm at 1100 nm, are well suited with the broadband scattering characteristic of the aerosol signal. ALI measures scattered sunlight from 650-950 nm with a stratospheric balloon flight from Timmins Ontario in the fall of 2014.

A similar instrument, the Atmospheric Limb Tracker for the Investigation of the Upcoming Stratosphere (ALTIUS) is a Belgium instrument designed by Belgian Institute for Space Aeronomy and its goal is to measure trace gas concentrations from measuring light in the limb scatter geometry as well as solar, stellar, and planetary occultation (*Dekemper et al.*, 2012). ALTIUS is a multichannel instrument using three AOTFs with different wavelength bands. The three channels for ALTIUS are an ultraviolet, visible, and NIR with wavelength ranges of 250-450 nm, 450-900 nm, and 900-1800 nm respectively and each channel images the atmosphere with 2 spatial dimensions.

In this paper, the first section will outline the fundamental operation of the AOTF used within the ALI system. Following is a description of the optical design behind ALI including an ulterior optical design comparing the benefits and drawbacks between two optical layouts. An overview of ALI's maiden flight, including the conditions and trajectory of the flight, onboard the CNES CARMEN-2 gondola from the CSA balloon launch facility in Timmins, Ontario is

summarized. Post flight analysis of the data is presented including the measurements taken during the campaign, the calibration process, and a retrieval algorithm for aerosol extinction and particle size parameters is outlined and applied to the data from the balloon campaign.

2 Instrument Design

2.1 Acousto-Optical Tunable Filter

The primary filtering device behind ALI and the technology that allows two dimensional spatial imaging is the AOTF. It uses an acoustic wave, with its wavelength being determined by a Radio Frequency (RF), that is propagated through the crystal and forms a standing wave to create an effect similar to diffraction of a specific wavelength causing a filtering effect. The use of an AOTF for an imaging system has several distinct advantages due to its low mass, fast stabilization times of a few microseconds, and no moving parts.

Non-collinear acousto devices, which are devices where the input wave and acoustic wave are not aligned, with the use of birefringent materials with large apertures are used in imaging systems have been possible since the 1970s (*Chang, 1974*). Thanks to recent advancements of non-collinear AOTF technology these devices can be used efficiently in imaging systems including a more accurate tuning curve (*Georgiev et al., 2002*) and consideration in the physical design with increased driving power (*Voloshinov et al., 2007*) have allowed for greater resolution. To create the diffraction of a specific wavelength a momentum matching criteria must be held where the wave vectors of the acoustic wave match the difference of the incoming and diffracted light wave vectors as seen in Figure 1. This condition is known as the Bragg matching criteria and is given by

$$\mathbf{k}_i = \boldsymbol{\kappa} + \mathbf{k}_d \quad (1)$$

where $|\mathbf{k}_i| = \frac{2\pi n_i}{\lambda}$ is the wave number of the incoming light, $|\mathbf{k}_d| = \frac{2\pi n_d}{\lambda}$ is the wave number of the diffracted light, and $|\boldsymbol{\kappa}| = \frac{2\pi F}{\nu}$ is the wave number of the acousto wave. The parameters λ , F , and ν are the wavelength in vacuum, the frequency of the RF wave, and the phase velocity in the crystal respectively. Using the condition given in Equation 1 and the wave vector diagram

gives the following relation for a birefringent material undergoing Bragg diffraction

$$\lambda = \frac{\Delta n \nu}{F} \frac{\sin^2(\theta_i + \alpha)}{\sin \theta_i} \quad (2)$$

where Δn is the absolute difference between the ordinary and extraordinary indices of refraction, θ_i is the angle of incidence of the incoming light, and α is the angle the acoustic wave propagates through the device. This equation has several implications to the operation of the device, first the wavelength diffracted by the AOTF is inversely related to frequency of the RF wave. Second, the wavelength of outgoing signal is dependant the angle of incidence of the incoming wave therefore passing a signal through the AOTF at different incident angles will result in a different outgoing wavelengths. Also, through the described interaction the diffracted light goes through a 90° rotation in polarization (*Voloshinov*, 1996).

A 10x10 mm aperture imaging quality ATOF was acquired from Brimrose of America. It is optically tuned, meaning designed for a specific wavelength octave, for a range of 600 to 1200 nm corresponding to a RF range of 156 to 70 MHz. It is made from Tellurium Dioxide (TeO₂), a birefringent crystal with indices of refraction at 800 nm of 2.226 and 2.373 for the ordinary and extraordinary modes respectively (*Uchida*, 1971). The extraordinary light is diffracted 2.7 degrees from the optical axis of the device. In order to achieve a constant diffraction angle the rear surface of the crystal is cut in a wedge shape to compensate for the angular change that occurs from altering the wavelength. The ordinary light undergoes diffraction but at a nonconstant angle from the optical axis with respect to wavelength. It is important to note that it is not possible to have both polarizations compensated and ALI is designed to measure the extraordinary polarization.

2.2 AOTF Characterization

The relationship between the RF tuning frequency, the central wavelength, and the spectral Point Spread Function (PSF) was obtained by passing focused light through the AOTF in the lab. In this system, linear polarizers were inserted before and after the AOTF to remove unwanted polarizations. 100 mm plano-convex lenses were chosen for the front and back end lenses to optimally fill the AOTF aperture. The light source was a 100 W quartz-tungsten halogen bulb that was collimated and passed into the first lens. The light passes through the

AOTF focused then is re-collimated through the second lens. The signal enters a HORIBA iHR320 spectrometer with a spectral resolution of 1.175 nm. The spectral results were imaged on a Synapse 354308 front-illuminated CCD detector with 1024x256 pixels. Images were taken at a set of RFs spaced every 150 kHz from 75 MHz to 160 MHz. For each image the results are spectrally averaged across the rows and a typical result can be seen in Figure 2a. The maximum value of each image is taken to be the central wavelength through the AOTF at each respective RF.

The maximum values from each of the images were determined as well as the corresponding wavelengths for these values. It was noted that the wavelength versus RF curve (Figure 2c) appears to follow a power function of the form

$$F = a\lambda^b. \quad (3)$$

A linear least squares fit was preformed in log space finding the coefficients a and b . The fit provided an agreement better than 0.6% within the testing range. A better fit was found in the form of

$$F = a\lambda^{b+c \log \lambda}. \quad (4)$$

These results can be seen in Figure 2c and Figure 2d. The agreement of this form is less than 0.1% throughout the whole wavelength range and the determined RF and wavelength relation as determined as

$$F = \exp(19.793)\lambda^{-3.381+0.168 \log \lambda} \quad (5)$$

where λ is in nanometers and F is in MHz. It should be noted that even though the AOTF optical range is 600 nm to 1200 nm our analysis only measured wavelengths from 600 nm to 1080 nm due to the low quantum efficiency of the CCD beyond this range.

The same set of data was used to determine spectral PSF by finding the Full Width Half Max (FWHM) for each of the above determined wavelengths. These results are shown in Figure 2b. The AOTF spectral resolution is well within the limits that are required in order to determine aerosol extinction in the upper troposphere and lower stratosphere since aerosol is a broadband scatterer.

The diffraction efficiency was determined using two sets of data; the first set is the data used

to characterize the wavelength-RF dependance of the AOTF, the second set is a measurement of the light that was incident to the AOTF in the previous experiment. To acquire the incident data the AOTF and linear polarizer on the back end of the optical chain was removed. The light source is measured again with the spectrometer without the diffraction of the AOTF. By taking the ratio of the diffracted wavelength over the incident radiance the diffraction efficiency was determined. The determined diffraction efficiency is between 56% to 64% across the measured spectral range and should be noted that the diffraction efficiency changes with respect to incoming angle (*Xu and Stroud, 1992*).

2.3 Optical Design and Performance

The ALI prototype design and performance discussed in this work has been designed with balloon geometry in mind, accounting for a larger field of view to be able to image the desired range of 35 km vertically and horizontally. The eventual goal for an ALI based instrument is a satellite mission in a low earth orbit (approximately 600 km). A smaller field of view will be required to have the same 35x35 km field of view. For a stratospheric balloon at a float altitude of 35 km to be able to capture the entire range a field of view of 6° is required. However for a low earth orbit, to capture the same range a field of view of only 0.8° is required. A comparison of the two geometries can be seen in Figure 3.

The AOTF limits the optical system to only having two practical layouts since the incoming light must enter the device at less than the acceptance angle, which is the maximum angle light can enter the device and still undergo an efficient diffraction interaction. These two layouts are a telecentric and a telescopic system. The telescopic or afocal system causes a wavelength gradient to be formed across the field of view of the image whereas the telecentric design overcomes this problem but has a larger spectral FWHM (*Suhre et al., 2004*).

A telecentric layout on both the front and back end of the AOTF leads to focused light passing through the AOTF. The filtered image has a consistent central wavelength across the entire image with a larger spectral FWHM since the diffracted wavelength is dependent on incident angle as seen in Equation 2. This system does have two inherent issues. First, this method is sensitive to any surface defects of the crystal since the light enters the crystal in focused bundles. Second, an effect caused by a shift in the location of the imaging focal

plane occurs that is dependant on wavelength. This effect is caused by the inherent change of optical path length. The optical path between the first two lenes is a fixed distance, however the AOTF is made of TeO_2 or paratellurite and has a high index of refraction. The crystal also has a high dispersive property, or Abbe number, so the index of refraction depends on the wavelength. The dispersive nature gives an apparent change in the optical path length dependant on wavelength. The change in path length, d , is given by

$$d(\lambda) = \frac{n(\lambda) - 1}{n(\lambda)}t \quad (6)$$

which is derived from the physical geometry where $n(\lambda)$ is the index of refraction with a wavelength dependance and t is the thickness of the crystal. The AOTF crystal causes the optical path in air to be lengthened by d , and in order to compensate, the length, d , must be added to the path to account for the discrepancy, but this can only be accounted for a specific wavelength. Defocusing will occur at the image plane for all other wavelengths and in order to correct for this problem additional compensating optics would need to be added or the CCD would need to be actively moved as the wavelengths are being scanned.

In the telescopic system the AOTF has collimated light for each line of sight passing through the device and this has a few fundamental changes that alter the system's imaging quality. First, the light passing through the AOTF from a single line of sight enters the AOTF at the same angle, so the image will have a narrower spectral PSF than the telecentric counterpart. However, each line of sight will be diffracted with a different fundamental central wavelength due to the angular dependance in the AOTF Bragg diffraction (Equation 2). The final image has a smaller spectral bandpass but there will be a wavelength gradient radiating out from the center of the image. Second, since light now passes through the AOTF collimated, the focal point of the image no longer changes with wavelength. Instead a lateral displacement of each line of sight occurs based on the angle of incidence and the diffracted wavelength which causes a slight change in magnification of the final image. The lateral displacement that occurs is given by the following relation

$$\delta = (n(\lambda) - 1) \frac{t\theta}{n(\lambda)} \quad (7)$$

where δ is the displacement from the original path. This magnification is a negligible change overall amounting to a maximum 0.04 mm on the detector for the current ALI design.

The telescopic system offers the ability of having an image plane location that is not dependant on the wavelength being imaged and was the ultimate optical design chosen for ALI. A telecentric system would lead to an optical layout that would either require mechanical components to move the imaging plane, additional optical elements to counteract the change in the optical path, or have lower resolution spatially at some wavelengths. For the second solution, an alternative custom lens or prism would need to be created in order to counteract the defocusing effect of the AOTF which would be outside of scope for the simple prototype design desired for ALI. The telescopic design allows for higher spatial resolution, which aligns with the goal of imaging the fine structure of aerosol extinction on the order of hundreds of metres.

Another minor consideration for the system is the central wavelength of each line of sight is dependant upon the angle of incident on the AOTF crystal which results in a wavelength gradient in the final image. The shortest wavelength occurs in the center of the image and radiates outward towards longer wavelengths as apparent in Equation 2. Using the telescopic layout with a 6° field of view ALI would have a wavelength gradient of approximately 7 nm at 650 nm central wavelength and 11 nm at 950 nm, however for a space based instrument with a relatively smaller field of view the gradient could be reduced to as small as 2 nm across the whole image which, at worse, is slightly larger than the FWHM of the AOTF. This effect would be a significant problem for instruments measuring trace gases absorption lines, for example NO_2 , but aerosol scattering is a broadband spectral feature from the visible well into the IR. The wavelength dependent magnification mentioned earlier only amounts to a change of a approximately 0.4% in both directions from the inherent magnification from 650 nm to 950 nm and overall this change is considered negligible.

Therefore we have chosen a telescopic design. For ALI, a simple three lens optical layout was chosen for the system using Commercial Off-The-Shelf (COTS) components. Two lens before the AOTF to form the front end optics and one lens comprises the back end optics. Consideration was given when choosing the lenses with regard to aperture size in order to reach approximately one second exposure times during the mission. In order to be able to achieve

the increased light throughput a demagnification occurs in the front end optics resulting in a tightening of the collimated light bundles allowing more light to enter the aperture of the AOTF. A field stop is added at the intermediate imaging point between the first two lenses to help reduce unwanted signal from continuing through the optical chain. Before the light enters the AOTF a linear polarizer is used to remove the incoming horizontal or ordinary polarized light, which is the polarization that is not imaged by ALI, removing the 0th and 1st order horizontal polarization from propagating through the system. The diffracted wavelength undergoes a 90° rotation in polarization so a second linear polarizer at 90° to the first is used after the AOTF to remove the undiffracted beam. The diffracted light is 2.7° from the optical axis and to compensate, the rest of the optical chain after the AOTF is aligned with this direction. A final imaging lens forms the image of the signal on a QSI 616s CCD which has a 16 bit output with 1536×1024 $9 \mu\text{m}$ pixels with a 15 count error on the readout for typical operating temperatures. A ray tracing diagram for ALI's optical system was created using the CODE V optical design software and can be seen in Figure 4. Analysis of the final design was also performed using the CODE V optical design software to determine the minimum resolution required to achieve an MTF of 0.3 across the entire field of view. To achieve a minimum MTF of 0.3 across the entire field of view an average of 7 pixels is required making the average vertical and horizontal resolution of ALI across the entire field of view 210 m. The final optical specification for ALI can be found in Table 1. Due to contamination from the zeroth order beam, a loss of 1° horizontal field of view occurs on the right side of the field of view giving an effective field of view of 6° by 5° .

Effective focal length (mm)	74.3
Front optics magnification	0.67
Back optics magnification	1.27
Field of view ($^\circ$)	6.0×5.0
F-number	7.5
Image Size (mm)	9×7.5
Image Size (pixels)	1000×800
Resolved Image Size (averaged pixels)	143×114
Spectral Range (nm)	650-950

Table 1: ALI Final System Optical Parameters.

Another concern in the design of limb scatter instruments is the effect of out-of-field stray

light that contaminates the final measurement. A front end baffle was designed and built using a method that maximizes the percentage of out-of-field light that will encounter at least three surfaces before entering the aperture of ALI. To further reduce the unwanted signal the baffle maintains a height to pitch ratio greater than 0.5 (*Fischer et al.*, 2008).

A SolidWorks rendition of the completed version of ALI can be seen in Figure 5. ALI is tilted at 3° from the horizontal so the complete 6° vertical field of view spans from the tangent point to the ground to the float altitude. A diagram can be seen in Figure 3.

ALI is similar in design and concept to the Belgium instrument, ALTIUS, except ALTIUS uses a telecentric optical layout and is designed to measure atmospheric trace gases (*Dekemper et al.*, 2012). Trace gases have narrow absorption features that require higher spectral resolution. A telecentric layout will provide a constant wavelength across the whole field of view. The optical specifications are similar between the two instruments, however two key differences will be noted. First, by using a telescopic layout ALI's maximum field of view is determined by choosing lenses to ensure light enters ALI within the acceptance angle of the AOTF allowing for a larger possible field of view than on a telecentric system where the field view is defined by the aperture of the AOTF. Second, the $f/\#$ for ALTIUS is 14.32 compared to ALI's 7.5 which allows ALI to increase light throughput at the cost of slightly higher aberrations in the final image. The visible channel of ALTIUS was breadboarded and tested by imaging a smoke stack in order to determine NO_2 slant column density at 3.5 km away with a 10 second exposure times (*Dekemper et al.*, 2012). It was noted that improvements to the system would result from methods to reduce the amount of stray light that enters the ALTIUS system, as well as a reduction in the time in between measurements and an improvement in the flat-fielding and spectral calibrations of the instrument.

2.4 Calibration and Operational Software

With the completed ALI prototype, calibrations and software testing were performed on ALI. The calibrations were performed with the goal to convert the ALI measurements into radiances to be used in a retrieval algorithm, including the removal of dark current, stray light, and flat-fielding. Second, a description of the operation software used on ALI during the mission will be described.

An experiment to characterize the stray light of the overall system was performed. Two types of stray light have been defined for ALI; first the out-of-field stray light is radiance that enters the optical path that is outside of the measured field of view. Second is internal stray light which is caused by optical elements not completely absorbing or removing any undesired wavelengths and polarizations. Stray light removal has always been difficult in atmospheric instrumentation due to the difficulty in accurately discerning the signal in regards to the stray light contamination. Furthermore, ALI's optical system has additional unwanted light internal to the instrument because of the rejection of one of the polarizations due to the nature of the AOTF. The signal enters the optical system unpolarized, but only one polarization has a constant output angle from the AOTF. The light is first passed through a linear polarizer with an extinction ratio of at least 100,000:1 to remove the unwanted polarization. However a small percentage is not absorbed. Furthermore, a second linear polarizer is used after the AOTF to reject the undiffracted signal and once again a small percentage of this is not absorbed leading to potentially substantial stray light in the optical housing. However, the diffraction interaction only occurs when the RF signal is applied, so without the RF wave the recorded measurement will only contain the stray light in the system. Using this characteristic another experiment was devised to determine the stray light of the system. A 250 W quartz-tungsten light source was passed through a dispersing screen and into the entrance aperture of ALI filling the entire field of view. Using a variety of exposure times ranging from 0.1 s to 60 s and wavelengths from 650 to 950 nm in 25 nm intervals the incoming source was imaged twice for each unique combination; one image recorded with the AOTF in its off state, with no driving RF wave, and one with the ATOF in its on state, with the RF wave. Once all the images were acquired the DC offset was removed and the counts were divided by the exposure times to give counts per second. Essentially, the image with the AOTF off only contains stray light in the system, as previously stated, and the "AOTF on" image contains the stray light combined with the uniform signal from the light source. By subtracting the "AOTF-off" image from the "AOTF-on" image yields an image that just contains the desired signal. The resulting images were the brightest in the centre and experienced vignetting towards the edges. The vignetting is caused by the aperture of the AOTF. In order to be able to use this method during the balloon campaign all images captured will have a corresponding "AOTF-off" image recorded

as well.

To complete calibrations flat-fielding needs to be performed on the images to yield the radiances. The resulting images from the stray light removal experiment were used to determine the coefficients for flat fielding. The coefficients were found in two steps. First, the spatial coefficients needed to be found for each individual image and second the spectral coefficients needed to be determined across wavelength. The spatial coefficients were found by determining the value needed to scale each pixel up to the average measurement of the center 25 by 25 pixels of each image. The images were sorted by wavelength and each set of scaled image values was noted to be within 4% of each other. The spatial coefficients for each set were averaged to find the final spatial coefficients for each wavelength with a 4% error. Second the spectral dependence was determined. ALI is most sensitive at 775 nm so this wavelength was chosen as the reference wavelength and all coefficients were scaled to yield the same value as the 775 nm spatially flat fielded images. The choice to relatively calibrate the ALI radiances to the 775 nm value was performed since no absolute calibration was performed on ALI. The final flat-fielding coefficients were the spatial times the spectral coefficients. The final images radiances are called relative radiance since the results are not absolutely calibrated.

During the calibration process software was designed for the ALI system to be used for the balloon campaign. ALI was operated with a Debian Linux operating system with threaded C++ based software to control the hardware and science operations that would initiate with system power on. The onboard computer was a VersaLogic PC-104 OCELOT computer with fanless operation and a 1.6 GHz Intel Atom processor with 2 GB of RAM and has a thermal operating range of -40 to 85°C. The onboard system communicated to a ground based station through UDP protocol and sends data, including images and house keeping information, to the ground, as well as receives commands from ground control.

3 Stratospheric Balloon Flight

3.1 Flight Day Conditions and Flight Path

The balloon launch base in Timmins, Ontario is located at 48.47°N 81.33°W and ALI was integrated onto the CNES CARMEN-2 gondola with CARMEN-2's systems, including com-

munications and power. ALI was orientated so it would be 90° from the azimuthal direction of the sun with an overall southern field of view during the mission. ALI measures light that is polarized vertically and computed values shows the vertical polarization only accounts for 10 to 35% of the total incoming radiance for the balloon geometry. CARMEN-2 is a pointed gondola and its pointing precision is better than $1'$ with the use of an onboard star tracker.

On September 20, 2014 at 05:35 UTC (01:35 local time) ALI was launched as part of the Nimbus 7 mission from the CSA Timmins balloon launch facility. During the launch, the sky was clear with light winds allowing for a safe and uneventful launch. The ascent of CARMEN-2 occurred in darkness and reached its flight altitude of 36.5 km at 8:17 UTC. First light was observed by ALI at 9:39 UTC and recorded measurements until 14:42 UTC when the primary aerosol observations were complete and ALI was powered off at 17:15 UTC. A visualization of the flight path with major landmarks noted can be found on Figure 6a. Temperature profiles for the ambient atmosphere and instrument can be seen in Figure 6b. The black curve is the ambient atmospheric temperature surrounding the gondola during the flight from the ECMWF (*Molteni et al.*, 1996). The blue, green, and red are from temperature sensors onboard ALI located on the baffle, camera, and RF driver respectively. The baffle temperature sensor was attached just on the inside of the ALI right by the entrance aperture for the system and monitors the temperature at the front of the system. The camera sensor is attached to the back of the CCD camera and the RF driver sensor measures the temperature of the RF driver which is used to control the AOTF. ALI was thermally insulated with foam to keep the system warm, while at the same time direct heating from the sun was a concern so the system was covered in a reflecting material to reduce solar heating.

During the mission, ALI operated in two primary acquisition modes, a “dark” mode and an aerosol imaging mode. The first mode, the “dark” mode, was primarily used during ascent and intermittently between aerosol modes. During this mode the filtering of the AOTF was disabled, meaning no RF signal is applied to the crystal, and the system images stay light and dark current. Eight exposures are taken with 0.05, 0.1, 0.5, 1, 2, 3, 5, 10 second exposure times with the camera shutter operating. The second operational mode, the aerosol mode, recorded 13 measurements at selected wavelengths every 25 nm between 650 to 950 nm. Each measurement is then a pair of images, an “AOTF-on” and “AOTF-off” image. Each measurement set

took approximately 35 s to acquire with exposure time varying between 0.5 to 6 seconds.

3.2 Measurements

After the successful recovery of ALI 216 raw images were download (known as the level 0 data) and calibration was performed to convert them into relative radiances (level 1 data) using the calibration methods discussed in subsection 2.4, removing the DC offset, stray light, and the application of the flat fielding coefficients. An example of an image with all calibrations applied can be seen in Figure 7a. This is image number 212 at 750 nm.

To increase the precision of the measurements to a minimum of 0.3 MTF from the flight the images were averaged in cells of 25 horizontal pixels and vertical pixels resulting in the measured radiances on a 1 km grid. ALI radiance profiles from the complete mission from the center column of the detector are shown in Figure 8. This includes wavelengths from 675-950 nm. The first set of radiance profiles that start near zero and move toward the large values are the radiance profiles that were recorded during sunrise and the gradual increase was therefore expected. Once the sun had completely risen past the terminator the relative radiance vectors follow a similar shape and have a similar magnitude with some variability corresponding largely to thin clouds. Image 212 was selected to demonstrate radiance differences between different horizontal lines of sight which can be seen in Figure 7b. The anomaly is determined by calculating the mean vertical relative radiance profile and removing it across the field of view. These clouds were formed after sunrise and appeared to be optically thin and formed in thin vertical layers only a kilometer in height and some high altitude stray light appears in the final image. Lastly, images 204 to 216 were used to show the spectrum of relative radiances at a series of altitudes which is seen in Figure 9 with the error of the relative radiances represented by the shading. The level 1 radiance data can now be used in the retrieval process.

3.3 Retrievals

The modeled radiances for the nonlinear inversion were computed with the SASKTRAN radiative transfer engine (*Bourassa et al., 2008a*) for High Resolution (SASKTRAN-HR) (*Zawada et al., 2015*) measurements using the newly developed polarization module (*Dueck S. and Degenstein*). The model uses a given atmospheric state to solve the radiative transfer equation

to determine the final radiance at the observer that follows the integral radiative transfer equation:

$$\mathbf{I}(s_1) = \mathbf{I}(s_0)e^{-\tau(s_0,s_1)} + \int_{s_0}^{s_1} k(s)\mathbf{J}(s)e^{-\tau(s,s_1)}ds \quad (8)$$

where $\mathbf{I}(s_1)$ is the vector radiance at the observer through a path from s_0 to s_1 , the first term is the contribution of light that is attenuated along the line of sight from the sun to the observer at s_1 . The second term takes the vector source term, $\mathbf{J}(s)$, which is the radiance scattered into the line of sight, and integrates the path along line of sight with attenuation to determine the scattering contribution to the final radiance. The extinction, given by $k(s)$, is the sum of the number density, $n(s)$, multiplied by the scattering cross section, $\sigma(s)$, over all species and τ is the optical depth. Furthermore SASKTRAN-HR uses a complete spherical geometry and accounts for multiple scattering terms. The polarized output of SASKTRAN-HR gives the Stokes vectors for the radiance on the model reference frame which can then be rotated into the instrument's coordinate system. Once rotated the polarization required to match the ALI measurement is the vertical polarization given by

$$I = \frac{1}{2}(S_0 - S_1) \quad (9)$$

where S_0 and S_1 are Stokes parameters defined by $S_0 = \langle E_x^2 \rangle + \langle E_y^2 \rangle$ and $S_1 = \langle E_x^2 \rangle - \langle E_y^2 \rangle$. The variables E_x and E_y are the horizontal and vertical component of the electric field in the instrument frame.

The relative radiance level 1 data from ALI are used to create measurement vectors, \mathbf{y} , in the following form

$$\mathbf{y} = \log \left(\frac{\mathbf{I}(\mathbf{z}, \lambda)}{I(z_{ref}, \lambda)} \right) - \log \left(\frac{\mathbf{I}_{rayleigh}(\mathbf{z}, \lambda)}{I_{rayleigh}(z_{ref}, \lambda)} \right) \quad (10)$$

where $\mathbf{I}(\mathbf{z}, \lambda)$ is the measured radiance from ALI and $I(z_{ref}, \lambda)$ is the radiance at a reference altitude used to normalize the signal from a high altitude where there is little aerosol contribution, for ALI the highest possible altitude where the signal is above the noise threshold is approximately 30 km tangent height. The second term uses modeled radiances from SASKTRAN-HR with only the molecular atmosphere to approximately remove the Rayleigh signal. This is done to improve the speed of the convergence of the retrieval. The ALI mea-

surement vector is similar to the measurement vector used for the OSIRIS retrieval (*Bourassa et al.*, 2007; *Bourassa et al.*, 2011). An initial guess state, \mathbf{x} , for the aerosol extinction and particle size distribution profiles are set in the SASKTRAN-HR model. The forward model vector is constructed similarly to the measurement vector and follows.

$$\mathbf{F}(\mathbf{x}, \mathbf{z}) = \log \left(\frac{\mathbf{I}_{mod}(\mathbf{z}, \lambda)}{I_{mod}(z_{ref}, \lambda)} \right) - \log \left(\frac{\mathbf{I}_{rayleigh}(\mathbf{z}, \lambda)}{I_{rayleigh}(z_{ref}, \lambda)} \right) \quad (11)$$

where $\mathbf{I}_{mod}(\mathbf{z}, \lambda)$ is the modeled radiance for the measurement and $I_{mod}(z_{ref}, \lambda)$ is the measurement at the same reference altitude for normalization. The forward model is used in combination with the measurement vector to update the extinction profile using Multiplicative Algebraic Reconstruction Technique (MART) algorithm which was developed for use in the OSIRIS retrievals (*Bourassa et al.*, 2012b) with the following iterative technique

$$x_i^{n+1} = x_i^n \sum_j \frac{y_j}{F(z_j)} W_{ij} \quad (12)$$

where x_i is the aerosol extinction at each shell altitude, i and j is the tangent point from the measurements. W_{ij} is the weighting matrix that relates the importance of each measurement vector to each shell altitude. This method was outlined by *Degenstein et al.* (2009) and allows for fast retrievals without calculating a Jacobian which can be computationally expensive for limb scatter.

An error estimation was performed using a perturbation method (*Bourassa et al.*, 2012a). Once a retrieval has been completed for an image the result is used to estimate the error in the returned extinction. For each altitude, the measurement vector is perturbed and the change in the retrieved profile is determined, a gain matrix, \mathbf{G} , is created comprised of the change in the extinction over the change in the measurement vector. The gain matrix has size n by m which are the shell altitudes and the tangent altitudes grids respectively. The error at each retrieved altitude is then given by

$$\mathbf{E} = \mathbf{G} \mathbf{S}_\epsilon \mathbf{G}^T \quad (13)$$

where \mathbf{S}_ϵ is the covariance matrix of the measurement vector and \mathbf{E} is the covariance of the retrieved aerosol profile. The precision for ALI is taken as the square root of the diagonal of \mathbf{E} (*Rodgers*, 2000).

Once the retrieval has been preformed for a complete series of wavelengths; determination of the Angström exponent is preformed in a similar method as outlined by *Rault and Loughman* (2013) for the OMPS aerosol particle size retrieval. The method outlined by *Rieger et al.* (2014) is not used due to ALI not measuring long enough wavelengths. The Angström exponent is an approximation to the spectral dependance of the Mie scattering cross section. Lower Angström exponents correspond to larger particle sizes and vice versa for small particle sizes. The scattering cross section for aerosol is dependant on the particle size distribution, and since the number density must be a constant across wavelength, the extinction changes with a change in cross section. From Equation 14 the particle size profile from a series wavelength can be determined from the Angström exponent. Since the measurements observe relatively the same atmosphere over the time of one complete aerosol cycle; the differences between extinction ratios at the different wavelength can be used to gather a understanding of aerosol particle size in the form

$$\frac{n\sigma}{n_0\sigma_0} = \left(\frac{\lambda}{\lambda_0}\right)^{-\alpha} \quad (14)$$

which characterizes the cross section particle size dependance verses wavelength where n is the aerosol concentration, and σ is the scattering cross section. For the retrieval described here a single mode log-normal distribution is assumed with a mode radius, r_g , and the mode width, σ_g , which is the same as the OSIRIS version 5.07 aerosol product. At each retrieved altitude the extinction from each wavelength is used to fit the Angström exponent. Then the median value from all the retrieved altitudes is used as the new size parameters in next iteration of the retrieval. The mode width is set at a constant 1.6 and the mode radius is allowed to vary to match the Angström exponent retrieved (*Bourassa et al.*, 2008b; *Rieger et al.*, 2014). The mode radius is updated and the process is repeated, re-retrieving the extinction profiles, until the Angström exponent converges. At the end of the last iteration, the Angström exponent profile is reported as the final particle size product.

In order to be able to use the ALI data in the MART method certain quantities were needed for the model; albedo, ozone concentration and cross sections, and aerosol cross sections. The ozone absorbtion features from the Chappuis band appear in the ALI measurements from 650 to 700 nm. The ozone profiles were acquired from OSIRIS. Five scans that were within 48 hours of the balloon flight and within 500 km of the launch facility were averaged together to be

the ozone profile used in the SASKTRAN-HR model, with cross sections from *Burrows et al.* (1999). The albedo is from the ADAM database which has monthly values for albedo over the surface on earth at a resolution of $0.1^\circ \times 0.1^\circ$ grid at 1 nm spectral resolution (*Muller et al.*, 2013). The aerosol cross sections come from the Mie scattering derivation that was originally proposed by Mie and was implemented efficiently by *Wiscombe* (1980). For the purpose of the retrieval an initial guess profile was used with a constant mode radius of $0.08 \mu\text{m}$ and a mode width of 1.6 which is considered a standard size distribution for aerosol (*Deshler et al.*, 2003).

3.4 Results

The complete mission consisted of 216 images that were recorded in illuminated conditions. The MART retrieval method was run on a select set for the purpose of the analysis, specifically the last complete set of images from 650 to 950 nm consisting of images 204-216. The complete set of retrieved aerosol extinction profiles can be seen in the left panel of Figure 10. After the retrieval the difference between the measurement and forward model vectors were less than 2% for the majority of the retrieval region, approximately 13 km to 24 km, across all wavelengths. From the retrieval altitudes the aerosol extinction shows a decrease as the wavelength increases which is expected due to the dependance of the cross section with respect to particle size.

The aerosol profile for the ALI 750 nm aerosol extinction is shown in blue with the shading representing the precision of the retrieved profile on the right of Figure 10. The error is strictly based on measurement error and neglects any model and atmospheric state errors. The green curve is the average 750 nm aerosol extinction profiles of the same five OSIRIS scans used for the ozone profile and red is the 750 nm aerosol extinction from SALOMON (*Berthet et al.*, 2002) which was launched from the Timmins balloon base as the Nimbus 5 mission on September 12, 2014. The aerosol extinction for ALI and OSIRIS are within 50% of each other for a majority of the 750 nm profile and is the wavelength where agreement is best. It also should be noted that the three instruments follow the same overall profile shape. First, a bend in the profile occurs at approximately 25 km, then increases approximately linearly until 15 km where aerosol extinction leaves the linear trend and forms the peak of the measurement.

The particle size method was used as outlined in the pervious section. The first panel of

Figure 11 shows the median Angström exponent that was determined after each iteration and convergence can be seen after a couple iterations. The particle size determined for ALI in the last complete set of aerosol images can be seen in the second panel of Figure 11 which yields a final Angström exponent of between 2 and 3 throughout the altitude range from 13 to 22 km. Assuming a mode width of 1.6 yields a median mode radius of 0.096 μm .

In order to determine the Angström exponent a least squares fit was used for all wavelengths at each altitude. A wavelength at an altitude was rejected if the forward model at that shell altitude was not within 2% of the measurement vector. In the case shown in Figure 11, the 20.5 km shell altitude, only 10 of the 13 possible wavelengths contributed to the determination of the Angström exponent.

4 Conclusions and Future Prospects

A description of the ALI prototype using an AOTF for active filtering in the visible to near IR with a telescopic optical layout with the purpose to measure aerosol extinction from the upper troposphere and lower stratosphere with a high vertical and horizontal resolution with images was presented here. The AOTF has fast stabilization times and the ability to disable the filter gives an excellent method to remove stray light from the final measurements. ALI is able to measure aerosol microphysics in atmospheric remote sensing.

ALI was tested on board the CARMEN-2 gondola from the balloon launch facility at Timmins, Ontario. Aerosol extinction profiles were determined and had good comparisons to ORISIS and SALOMON in profile shape. The absolute extinction values are different by a large amounts but can be attributed to the large amount of unaccounted systematics in the retrieval algorithm. Overall, ALI preformed admirably and verified the use of this technology for future atmospheric remote sensing missions.

Future upgrades to ALI would include the realignment of the optics for flight temperatures to allow for higher resolution measurements and retrievals. Secondly, replacing the CCD currently used on ALI with a camera with faster readout would allow for a higher quantity of data to be taken by reducing the approximate 35 s readout time down to a smaller value necessary for a satellite missions on the order of 1 s per wavelength.

This work would have not been possible without funding from the CSA to design and

build ALI through the FAST program as well as the CSA building and managing the launch facility in Timmins, Ontario. Also, thanks to CNES for funding and overseeing the launches at Timmins in 2014. As well thanks Nick Lloyd for help in development of the flight code, without his efforts this work would have not been accomplished.

References

- Barth, C., D. Rusch, R. Thomas, G. Mount, G. Rottman, G. Thomas, R. Sanders, and G. Lawrence (1983), Solar mesosphere explorer: Scientific objectives and results, *Geophysical research letters*, *10*, 237–240.
- Berthet, G., J.-B. Renard, C. Brogniez, C. Robert, M. Chartier, and M. Pirre (2002), Optical and physical properties of stratospheric aerosols from balloon measurements in the visible and near-infrared domains. i. analysis of aerosol extinction spectra from the amon and salomon balloonborne spectrometers, *Applied optics*, *41*, 7522–7539.
- Bourassa, A. E., D. A. Degenstein, R. L. Gattinger, and E. J. Llewellyn (2007), Stratospheric aerosol retrieval with optical spectrograph and infrared imaging system limb scatter measurements, *Journal of Geophysical Research (Atmospheres)*, *112*, D10217, doi:10.1029/2006JD008079.
- Bourassa, A. E., D. A. Degenstein, and E. J. Llewellyn (2008a), SASKTRAN: A spherical geometry radiative transfer code for efficient estimation of limb scattered sunlight, *Journal of Quantitative Spectroscopy and Radiative Transfer*, *109*, 52–73, doi:10.1016/j.jqsrt.2007.07.007.
- Bourassa, A. E., D. A. Degenstein, and E. J. Llewellyn (2008b), Retrieval of stratospheric aerosol size information from OSIRIS limb scattered sunlight spectra, *Atmospheric Chemistry & Physics*, *8*, 6375–6380.
- Bourassa, A. E., C. A. McLinden, C. E. Sioris, S. Brohede, A. F. Bathgate, E. J. Llewellyn, and D. A. Degenstein (2011), Fast no₂ retrievals from odin-osiris limb scatter measurements, *Atmospheric Measurement Techniques*, *4*, 965–972, doi:10.5194/amt-4-965-2011.

- Bourassa, A. E., C. A. McLinden, A. F. Bathgate, B. J. Elash, and D. A. Degenstein (2012a), Precision estimate for Odin-OSIRIS limb scatter retrievals, *Journal of Geophysical Research (Atmospheres)*, *117*, D04303, doi:10.1029/2011JD016976.
- Bourassa, A. E., L. A. Rieger, N. D. Lloyd, and D. A. Degenstein (2012b), Odin-OSIRIS stratospheric aerosol data product and SAGE III intercomparison, *Atmospheric Chemistry & Physics*, *12*, 605–614, doi:10.5194/acp-12-605-2012.
- Bourassa, A. E., A. Robock, W. J. Randel, T. Deshler, L. A. Rieger, N. D. Lloyd, E. T. Llewellyn, and D. A. Degenstein (2012), Large volcanic aerosol load in the stratosphere linked to asian monsoon transport, *Science*, *337*, 78–81.
- Bovensmann, H., J. Burrows, M. Buchwitz, J. Frerick, S. Noël, V. Rozanov, K. Chance, and A. Goede (1999), Sciamachy: Mission objectives and measurement modes, *Journal of the Atmospheric Sciences*, *56*, 127–150.
- Burrows, J., A. Richter, A. Dehn, B. Deters, S. Himmelmann, S. Voigt, and J. Orphal (1999), Atmospheric remote-sensing reference data from gome2. temperature-dependent absorption cross sections of O_3 in the 231–794nm range, *Journal of Quantitative Spectroscopy and Radiative Transfer*, *61*, 509–517.
- Chang, I. C. (1974), Noncollinear acousto-optic filter with large angular aperture, *Applied Physics Letters*, *25*, 370, doi:10.1063/1.1655512.
- Degenstein, D., A. Bourassa, C. Roth, and E. Llewellyn (2009), Limb scatter ozone retrieval from 10 to 60 km using a multiplicative algebraic reconstruction technique, *Atmospheric Chemistry and Physics*, *9*, 6521–6529.
- Dekemper, E., N. Loodts, B. V. Opstal, J. Maes, F. Vanhellemont, N. Mateshvili, G. Franssens, D. Pieroux, C. Bingen, C. Robert, L. D. Vos, L. Aballea, and D. Fussen (2012), Tunable acousto-optic spectral imager for atmospheric composition measurements in the visible spectral domain, *Applied Optics*, *51*, 6259–6267, doi:10.1364/AO.51.006259.
- Deshler, T., M. Hervig, D. Hofmann, J. Rosen, and J. Liley (2003), Thirty years of in situ stratospheric aerosol size distribution measurements from laramie, wyoming (41 n), using

- balloon-borne instruments, *Journal of Geophysical Research: Atmospheres* (1984–2012), 108.
- Dueck S., A. E., Bourassa, and D. A. Degenstein (), SASKTRAN-HR Polarization Module, *In Preparations*.
- Ernst, F., C. von Savigny, A. Rozanov, V. Rozanov, K.-U. Eichmann, L. A. Brinkhoff, H. Bovensmann, and J. P. Burrows (2012), Global stratospheric aerosol extinction profile retrievals from sciamachy limb-scatter observations, *Atmospheric Measurement Techniques Discussions*, 5, 5993–6035, doi:10.5194/amtd-5-5993-2012.
- Fischer, H., M. Birk, C. Blom, B. Carli, M. Carlotti, T. v. Clarmann, L. Delbouille, A. Dudhia, D. Ehhalt, M. Endemann, et al. (2008), Mipas: an instrument for atmospheric and climate research, *Atmospheric Chemistry and Physics*, 8, 2151–2188.
- Georgiev, G., D. A. Glenar, and J. J. Hillman (2002), Spectral characterization of acousto-optic filters used in imaging spectroscopy, *Appl. Opt.*, 41, 209–217, doi:10.1364/AO.41.000209.
- Hofmann, D., J. Barnes, M. O’Neill, M. Trudeau, and R. Neely (2009), Increase in background stratospheric aerosol observed with lidar at mauna loa observatory and boulder, colorado, *Geophysical Research Letters*, 36, n/a–n/a, doi:10.1029/2009GL039008, 115808.
- Kiehl, J. T., and B. P. Briegleb (1993), The relative roles of sulfate aerosols and greenhouse gases in climate forcing, *Science*, 260, 311–314, doi:10.1126/science.260.5106.311.
- Llewellyn, E., N. D. Lloyd, D. A. Degenstein, R. L. Gattinger, S. V. Petelina, A. E. Bourassa, J. T. Wiensz, E. V. Ivanov, I. C. McDade, B. H. Solheim, J. C. McConnell, C. S. Haley, C. von Savigny, C. E. Sioris, C. A. McLinden, E. Griffioen, J. Kaminski, W. F. J. Evans, E. Puckrin, K. Strong, V. Wehrle, R. H. Hum, D. J. W. Kendall, J. Matsushita, D. P. Murtagh, S. Brohede, J. Stegman, G. Witt, G. Barnes, W. F. Payne, L. Piche, K. Smith, G. Warshaw, D. L. Deslauniers, P. Marchand, E. H. Richardson, R. A. King, I. Wevers, W. McCreath, E. Kyrola, L. Oikarinen, G. W. Leppelmeier, H. Auvinen, G. Megie, A. Hauchecorne, F. Lefevre, J. de La Noe, P. Ricaud, U. Frisk, F. Sjoberg, F. von Scheele, and L. Nordh (2004), The OSIRIS instrument on the Odin spacecraft, *Canadian Journal of Physics*, 82, 411–422, doi:10.1139/p04-005.

- McCormick, M. (1987), Sage ii: an overview, *Advances in space research*, 7, 219–226.
- McCormick, M., P. Hamill, W. Chu, T. Swissler, L. McMaster, and T. Pepin (1979), Satellite studies of the stratospheric aerosol, *Bulletin of the American meteorological Society*, 60, 1038–1046.
- Molteni, F., R. Buizza, T. N. Palmer, and T. Petroliaxis (1996), The ecmwf ensemble prediction system: Methodology and validation, *Quarterly Journal of the Royal Meteorological Society*, 122, 73–119.
- Muller, J.-P., P. Lewis, F.-M. Bréon, C. Bacour, I. Price, L. Chaumat, P. Prunet, L. Gonzales, C. Schlundt, M. Vountas, et al. (2013), A surface reflectance database for esas earth observation missions (adam), *Living Planet Symposium*.
- Neely, R. R., P. Yu, K. H. Rosenlof, O. B. Toon, J. S. Daniel, S. Solomon, and H. L. Miller (2014), The contribution of anthropogenic so₂ emissions to the asian tropopause aerosol layer, *Journal of Geophysical Research: Atmospheres*, 119, 1571–1579, doi:10.1002/2013JD020578.
- Rault, D. F., and R. P. Loughman (2013), The omps limb profiler environmental data record algorithm theoretical basis document and expected performance, *Geoscience and Remote Sensing, IEEE Transactions on*, 51, 2505–2527.
- Rieger, L. A., A. E. Bourassa, and D. A. Degenstein (2014), Stratospheric aerosol particle size information in odin-osiris limb scatter spectra, *Atmospheric Measurement Techniques*, 7, 507–522, doi:10.5194/amt-7-507-2014.
- Rodgers, C. (2000), *Inverse Methods for Atmospheric Sounding: Theory and Practice*, Series on atmospheric, oceanic and planetary physics: 1999, World Scientific.
- Solomon, S., J. S. Daniel, R. R. Neely, J.-P. Vernier, E. G. Dutton, and L. W. Thomason (2011), The persistently variable background stratospheric aerosol layer and global climate change, *Science*, 333, 866–870, doi:10.1126/science.1206027.
- Suhre, D. R., L. J. Denes, and N. Gupta (2004), Telecentric confocal optics for aberration

- correction of acousto-optic tunable filters, *Applied Optics*, *43*, 1255–1260, doi:10.1364/AO.43.001255.
- Thomason, L. W., and G. Taha (2003), Sage iii aerosol extinction measurements: Initial results, *Geophysical research letters*, *30*.
- Uchida, N. (1971), Optical properties of single-crystal paratellurite (TeO_2), *Phys. Rev. B*, *4*, 3736–3745, doi:10.1103/PhysRevB.4.3736.
- Vernier, J.-P., J.-P. Pommereau, A. Garnier, J. Pelon, N. Larsen, J. Nielsen, T. Christensen, F. Cairo, L. Thomason, T. Leblanc, et al. (2009), Tropical stratospheric aerosol layer from calipso lidar observations, *Journal of Geophysical Research: Atmospheres (1984–2012)*, *114*.
- Vernier, J.-P., L. W. Thomason, J.-P. Pommereau, A. Bourassa, J. Pelon, A. Garnier, A. Hauchecorne, L. Blanot, C. Trepte, D. Degenstein, and F. Vargas (2011), Major influence of tropical volcanic eruptions on the stratospheric aerosol layer during the last decade, *Geophysical Research Letters*, *38*, n/a–n/a, doi:10.1029/2011GL047563, 112807.
- Voloshinov, V. (1996), Spectral and polarization analysis of optical images by means of acousto-optics, *Optics Laser Technology*, *28*, 119–127, doi:10.1016/0030-3992(95)00079-8.
- Voloshinov, V. B., K. B. Yushkov, and B. B. J. Linde (2007), Improvement in performance of a TeO_2 acousto-optic imaging spectrometer, *Journal of Optics A: Pure and Applied Optics*, *9*, 341–347, doi:10.1088/1464-4258/9/4/006.
- Winker, D. M., J. R. Pelon, and M. P. McCormick (2003), The calipso mission: Spaceborne lidar for observation of aerosols and clouds, 1–11.
- Wiscombe, W. J. (1980), Improved mie scattering algorithms, *Applied optics*, *19*, 1505–1509.
- Xu, J., and R. Stroud (1992), *Acousto-optic devices: principles, design, and applications*, vol. 12, Wiley-Interscience.
- Zawada, D. J., S. R. Dueck, L. A. Rieger, A. E. Bourassa, N. D. Lloyd, and D. A. Degenstein (2015), High resolution and monte carlo additions to the sasktran radiative transfer model, *Atmospheric Measurement Techniques Discussions*, *8*, 3357–3397, doi:10.5194/amtd-8-3357-2015.

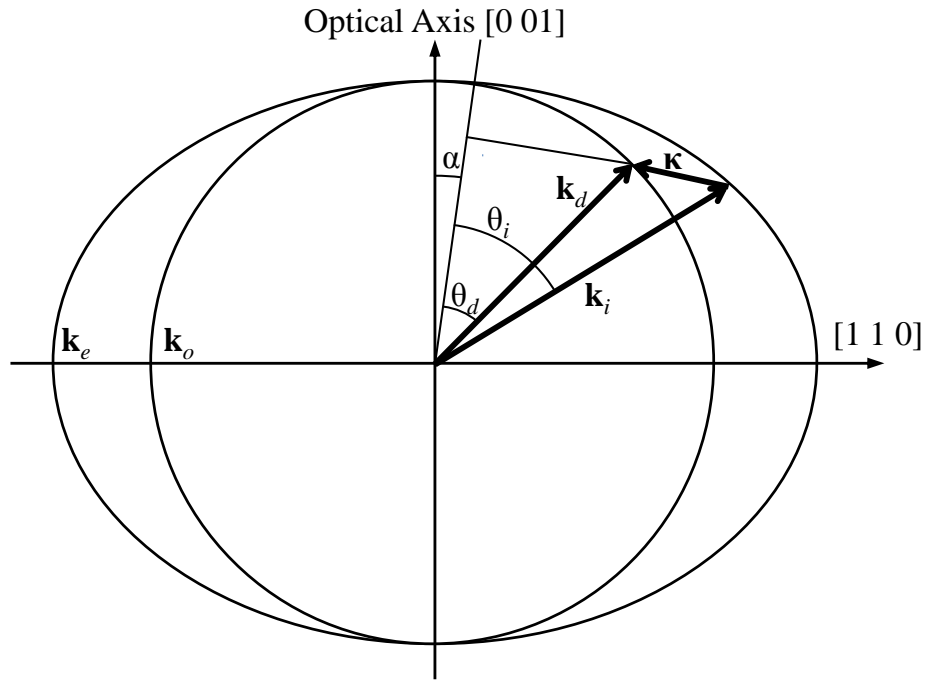


Figure 1: The wave vectors generated by the AOTF experiment. From Equation 1, the incident wave vector, diffracted wave vector, and acoustic wave vector are shown.

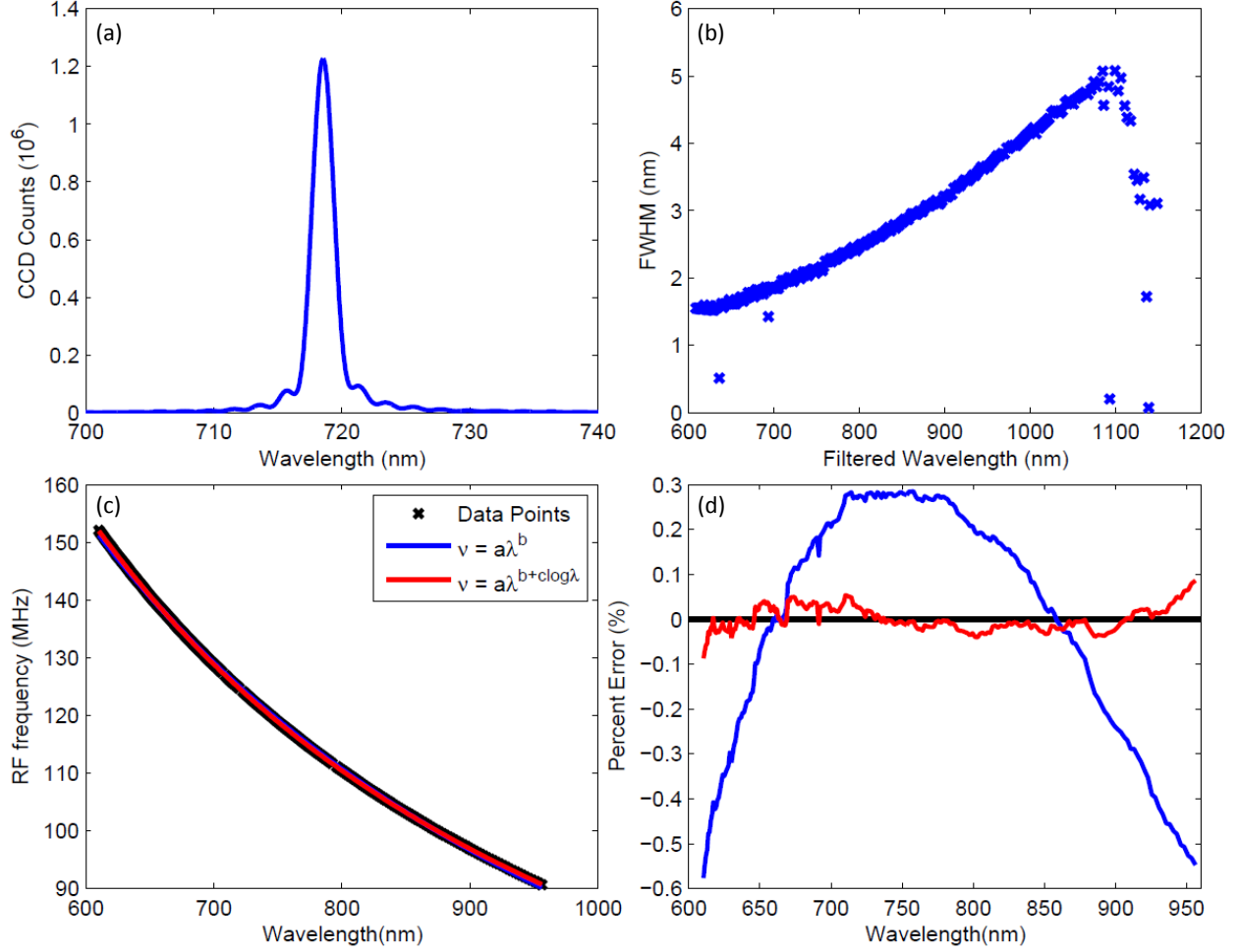


Figure 2: (a) A standard image taken from the AOTF calibration experiment when the tuning frequency of the AOTF was at 124.96 MHz. (b) The FWHM for each of the determined wavelengths for the AOTF. The FWHM at 600 nm is 1.5 and as the wavelengths get longer the FWHM increases to 4.9 at 1080 nm. (c) The calibration curves for the AOTF RF versus the diffracted wavelength which contains the data points recorded and two best fit curves. (d) The percent error with respect to the measured frequency for the two best fit curves in the previous panel.

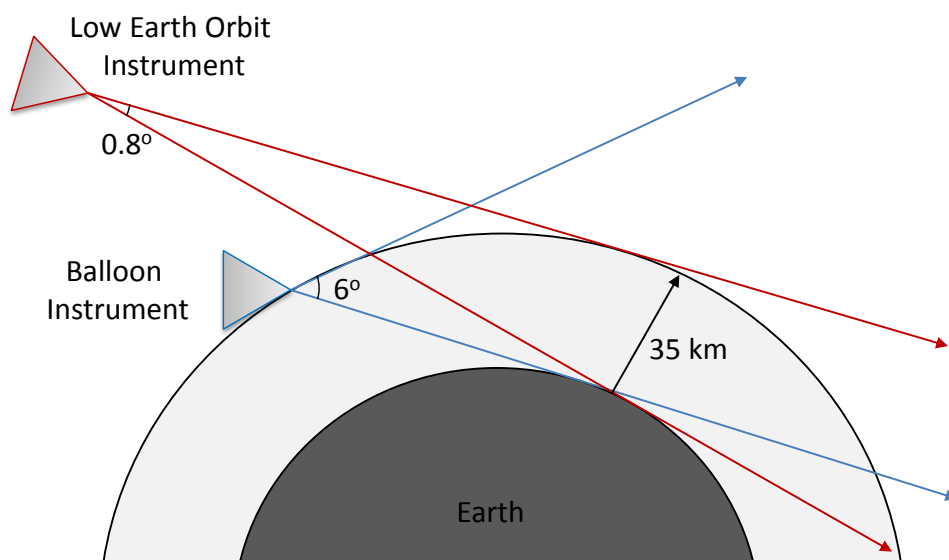


Figure 3: A comparison of ALI in a stratospheric balloon and low earth orbit satellite in blue and red respectively. In order to be able to gather the same vertical range of the limb a balloon geometry requires a 6° field of view at 35 km float altitude compared to a 0.8° field of view in a low earth orbit at 600 km.

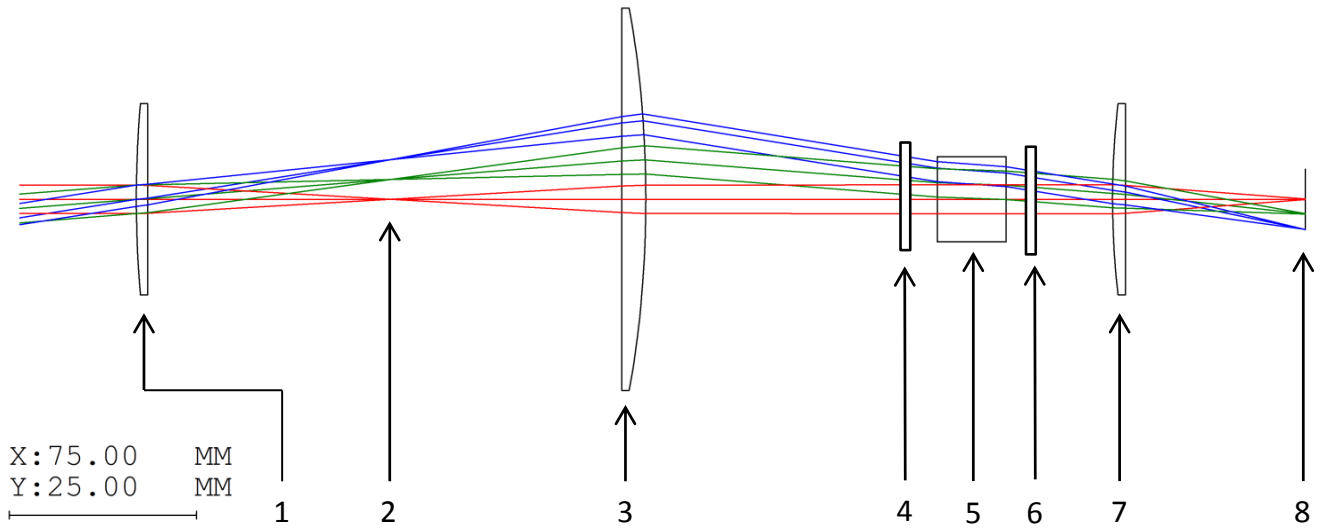


Figure 4: Ray Tracing diagram of the telescopic lens system for ALI simulated by Code V optical design software. The elements in the system are the following: (1) 150 mm focal length plano-convex lens. (2) Slit plate. (3) 100 mm focal length plano-convex lens. (4) Vertical linear polarizer. (5) Brimrose AOTF. (6) Horizontal linear polarizer. (7) 50.4 mm focal length plano-convex lens. (8) Imaging plane.

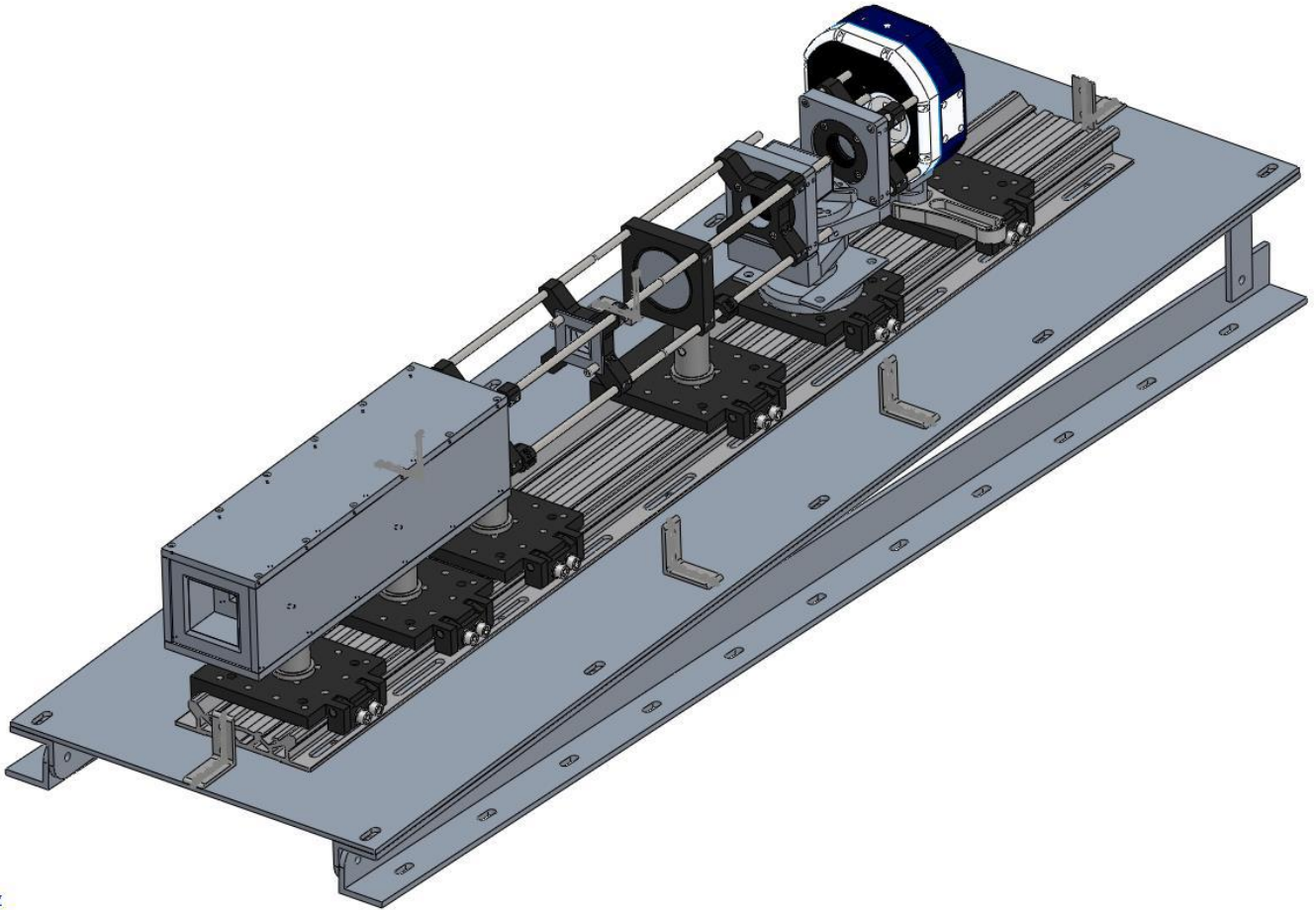


Figure 5: An isometric view of the complete ALI system with the baffle and 3° slant required to correctly position the field of view. Light tight case absent from diagram.

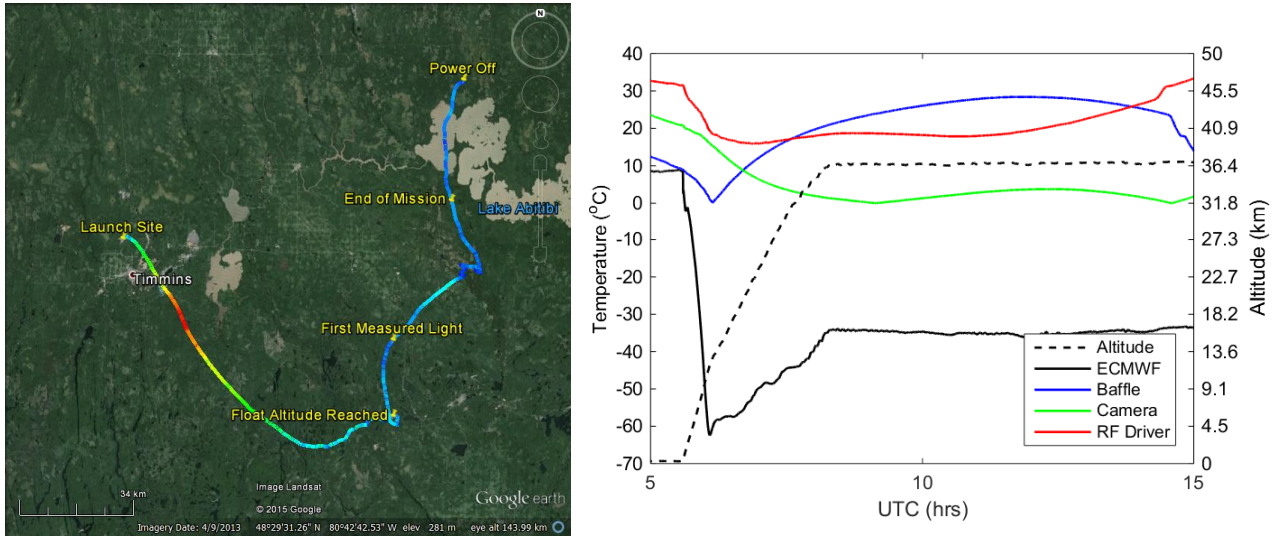


Figure 6: (A) The GPS data from ALI during the Nimbus 7 mission generated via Google Earth. The colour of the line represents the absolute speed of the gondola during the mission. Important landmarks are noted on the image. The end of mission represent the end of the aerosol mission. No GPS data was collected from ALI after power down. (B) The temperature and altitude profiles from the NIMBUS 7 flight.

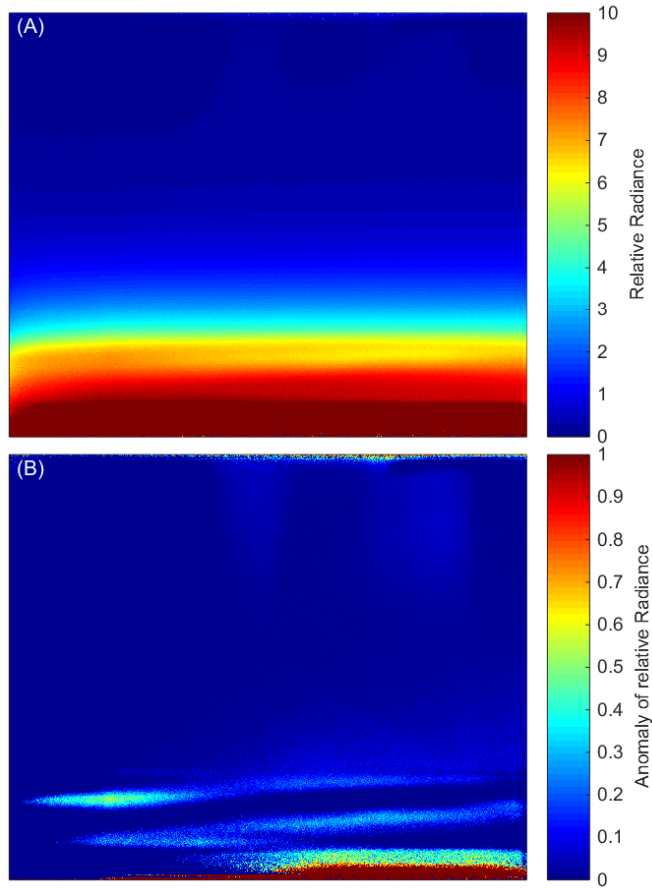


Figure 7: (A) Final calibrated 750 nm image, number 212. (B) The same 750 nm image with the mean of the profile removed from the image leaving the residual signal that shows thin clouds.

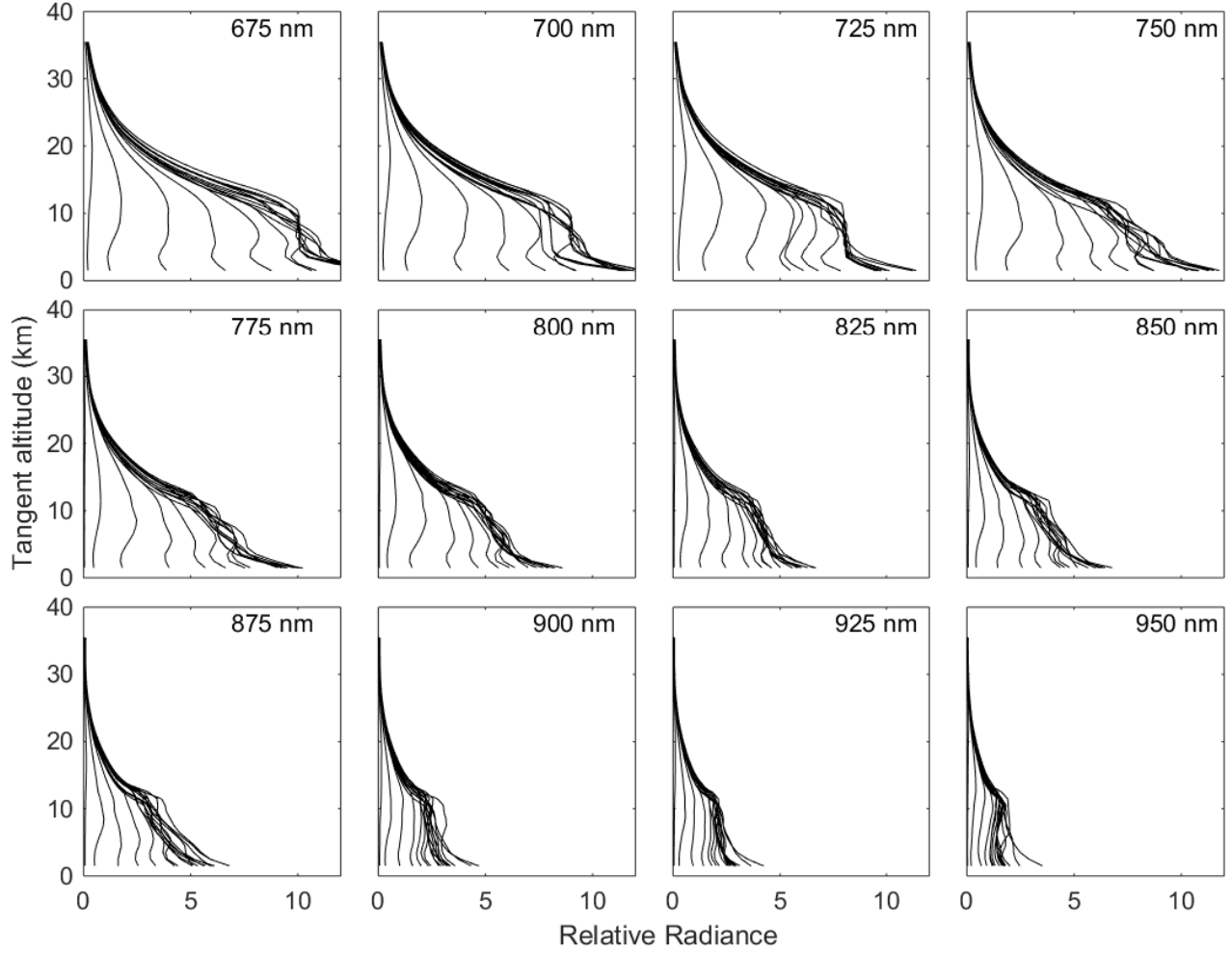


Figure 8: All ALI relative radiance vectors from the NIMBUS-7 flight from the straight ahead line of sight, the average of the centre 25 columns of pixels, averaged to a 1 km resolution. Each panel presents the radiance vectors from a different wavelength measured which is denoted in the top right corner.

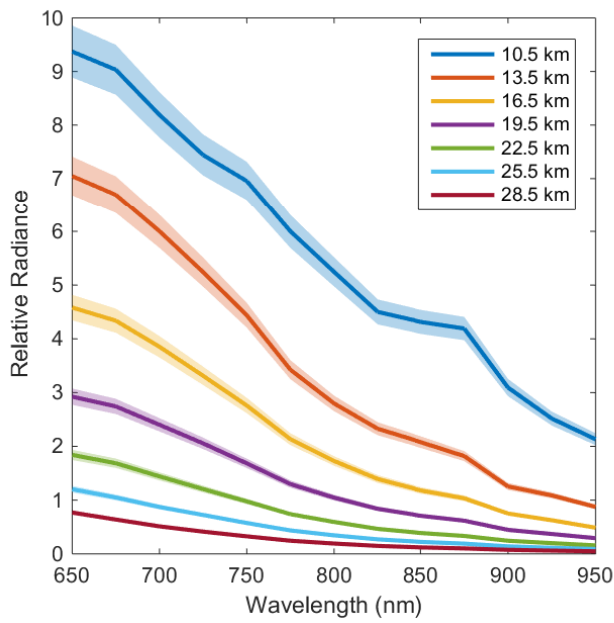


Figure 9: Level 1 relative radiances spectrally from 650 nm to 950 nm as measured from ALI at approximately 14:20 UTC consisting of images number 204 to 216 looking 90° in the azimuth from the sun facing southwards. These spectral profiles are presented at several tangent altitudes with a horizontal look direction of 0° . The shading represents the error on the radiances.

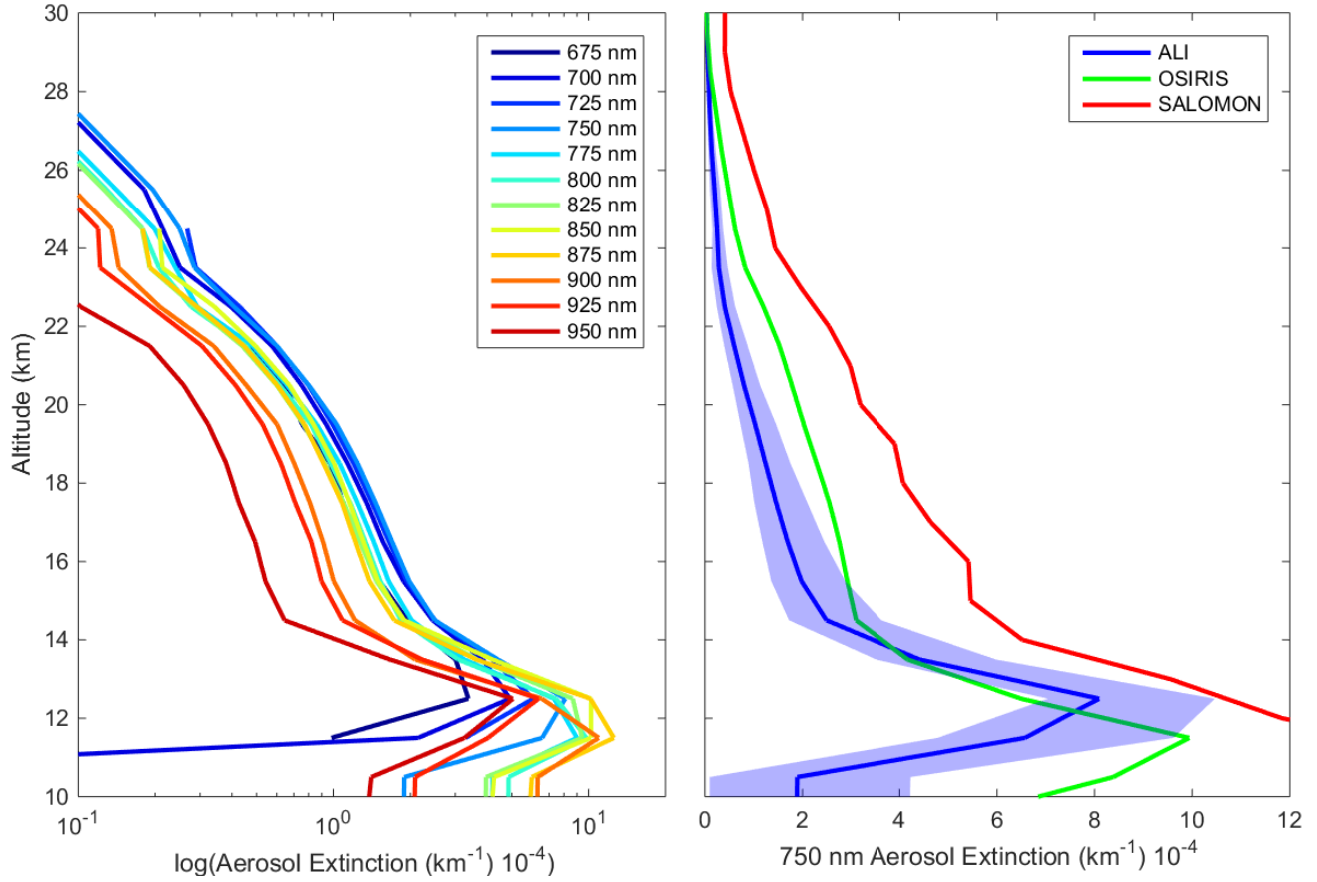


Figure 10: Left is the retrieved aerosol extinction profiles from the last complete imaging cycle consisting of images 205 to 216 from the 0.0° horizontal line of sight. Right is the 750 nm ALI aerosol extinction in blue with its error represented by the shading compared to the 750 nm extinction measured by OSIRIS and SALOMON in green and red respectively.

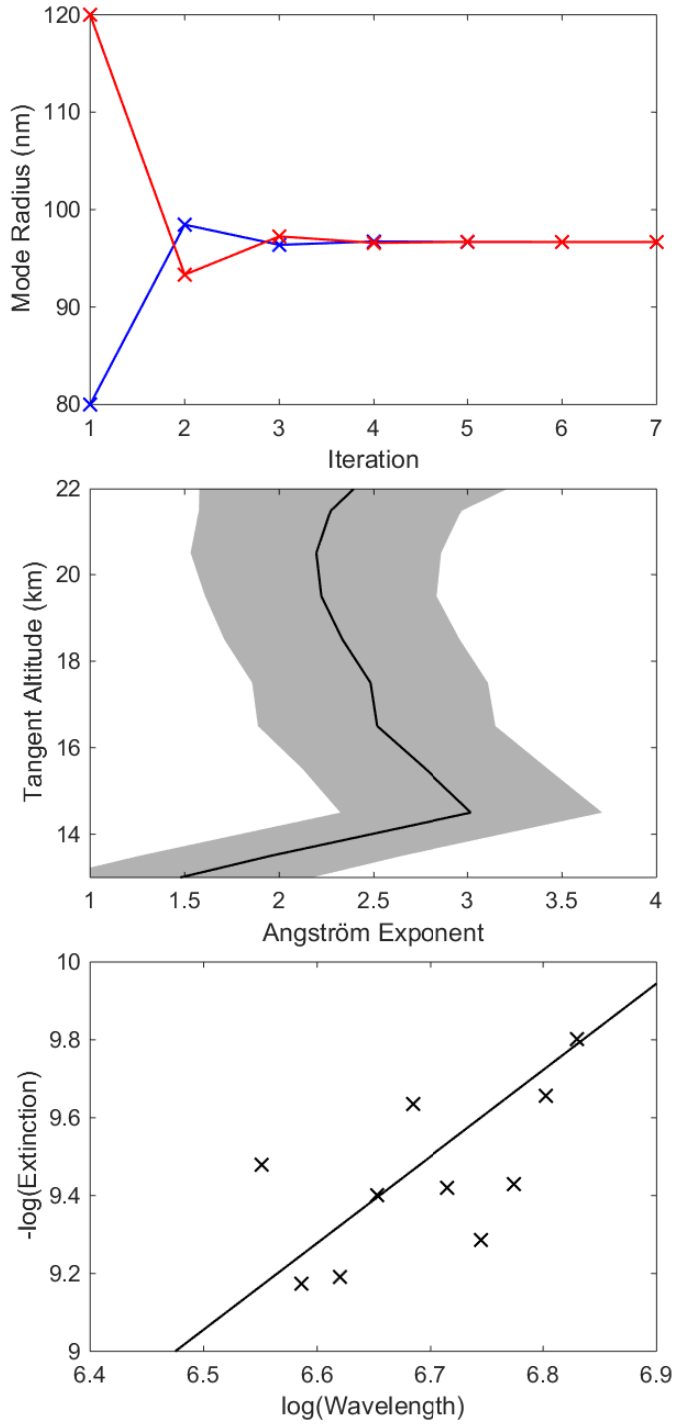


Figure 11: The top panel shows the convergence of two sample particle size retrievals over the iterations, blue and red represent an initial state of 0.08 and 0.12 μm respectively. Both initial states converge to the same value over approximately 4 iterations in the particle size retrieval method. The second panel is the final Angström exponents determined for images 204-216 during the Timmins 2014 campaign and the shading represents the error associated with the least squares fit. The last panel demonstrates a least squares fit to determine the Angström exponent at 20.5 km shell altitude.